Comparison between numerical simulation of semisolid flow into a die using FORGE© and in situ visualization using a transparent sided die

Adriana Neag, Véronique Favier, Régis Bigot, Helen Valerie Atkinson

Comparison between numerical simulation of semisolid flow into a die using FORGE© and *in situ* visualization using a transparent sided die

Adriana Neag[a,*], Veronique Favier[b], Regis Bigot[c], Helen Valerie Atkinson[d]

[a] *Department of Materials Science and Engineering, Technical University, Cluj-Napoca 400641, Romania*
[b] *Arts et Métiers ParisTech, PIMM UMR CNRS 8006, 75013 Paris, France*
[c] *Arts et Métiers ParisTech, LCFC, EA 4495, 57078 Metz Cedex 3, France*
[d] *Department of Engineering, University of Leicester, University Road, Leicester LE1 7RH, UK*

Keywords:
Semisolid
Thixoforming
Aluminum alloy
Friction
Numerical simulation

A B S T R A C T

Semi-solid processing is a promising forming process for shaping metallic alloys in one shot. Numerical simulations are of great interest for optimizing the process. Generally, numerical simulation results are compared with interrupted flow experiments but these do not fully reflect the progress of material into the die because of the inertia of the flowing material which continues to move after the interruption to the shot. Results are available for *in situ* visualization of flow using transparent sided dies. Here die filling with a 90° change of flow path was simulated using the FORGE© finite element code and a constitutive equation based on a micro-macro modelling approach. The predicted flow behaviour was compared to the *in situ* visualization images obtained with a transparent glass sided die and reported in the literature. The impact of the presence of an obstacle, ram speed and friction coefficients on the material flow front is discussed. The initial solid skeleton is broken as soon as the material is deformed. The effect of the ram speed on the flow front is successfully represented by keeping the same parameters for the constitutive laws but requires a change in the friction coefficients. Friction modelling using the Coulomb law limited by Tresca cannot represent the ram speed effect on experimental friction conditions for the *in situ* visualisation tests used for the comparison here. However, the effect of an obstacle within the die on the material flow front is predicted well.

1. Introduction

Semi-solid processing uses metallic alloys in the semi-solid state reached when alloys are heated to between the solidus and the liquidus. It exploits the thixotropic behaviour of such materials obtained when the solid phase has a spheroidal structure and firstly discovered at MIT by Flemings and co-workers (Spencer et al., 1972). Ito et al. (1992) observed that the solid particles can agglomerate even for moderate solid fractions. Flemings (1991) described that this agglomeration results in a more or less connected skeleton while the liquid phase may be entrapped in the solid phase or spatially continuous and free to flow. Deagglomeration of the solid phase and the induced change in spatial liquid-solid distribution during deformation are responsible for shear thinning and time-dependent behaviour.

The focus of this background literature survey is those more recent studies where simulation has been compared with experiment. Studies before 2005 are summarized in the review by Atkinson (2005). Numerical simulations require validation experiments. Conventionally for semi-solid processing this has been done with interrupted filling to check the intermediate position of the flow fronts (Atkinson, 2005). Comparisons also involve scrutiny of the load evolution during the process and of the solid fraction via the image analysis of the quenched microstructure. Hufschmidt et al. (2006) demonstrated the relevancy of two-phase constitutive models to reproduce the pressure evolution during filling of a T-shaped die with tin-lead alloy. They also showed that the experimental flow front is well reproduced for three piston velocities with a single set of parameters for two-phase simulations. However, the model parameters for one-phase simulation had to be readjusted to achieve satisfactory results for different piston velocities. Maciol (2009) simulated the same experiment by Hufschmidt

* Corresponding author.
E-mail addresses: adriana.neag@ipm.utcluj.ro (A. Neag), veronique.favier@ensam.eu (V. Favier), regis.bigot@ensam.eu (R. Bigot), hva2@le.ac.uk (H.V. Atkinson).

et al. (2006) using their own CFD code including the Internal Variable Convection methodology which is efficient for history dependent materials. A qualitative agreement between the experimental and computed flow front was found but the modelling requires further development. Solek et al. (2005) suggested that the discrepancies between the predicted and experimental load evolution during thixocasting of Al-Si alloy were due to the fact that the transient behaviour was ignored. Koeune and Ponthot (2014) simulated thixoextrusion and predicted load evolution with three different constitutive equations. The kinematics of the deformation were compared to the experimental results, including interrupted tests. The results also revealed the effectiveness of including transient and non-isothermal behaviour in the constitutive equations so achieving a better match between experiments and simulations. Kang et al. (2008) compared the predicted and experimental filling rates of a specifically designed die providing a gradual decrease of the piece thickness. The simulations were performed using the MAGMAsoft thixo-module. They showed that the gate width had a strong effect. Very recently, Jorstad et al. (2014) explained why semi-solid slurries can fill thin sections at seemingly unlimited flow velocity thanks to comparisons between experimental and computed filling of thin cast sections.

As reported by Atkinson (2005), *in situ* observation is the most appropriate way of checking the position of the flow front during die filling but generally dies are closed and opaque. The main recent work with transparent glass-sided dies enabling die filling to be filmed is that of Hufschmidt et al. (2006) and that reported by Atkinson et al. (2002) and published in Atkinson and Ward (2006). Hufschmidt et al. (2006) used a T-shaped die covered with a glass plate on one side and carried out isothermal experiments with Sn-12%Pb. Atkinson and Ward (2006) designed a set-up which can be used with both SnPb and aluminium alloys. In the latter case, experiments are not isothermal because of the experimental challenges of these higher temperatures. However, the die is heated, the speed is fast and the die section is relatively thick minimizing the tendency for solidification. Various obstacle shapes were placed in the path of the flowing material to observe flow fronts splitting and remerging.

In this work, the latter experiments (Atkinson et al., 2002; Atkinson and Ward, 2006) have been simulated using the FORGE© software. The predicted flow is compared to the experimental results in order to better understand the filling pattern. The impact of the presence of an obstacle, ram speed and friction conditions on the processing is discussed. For this purpose, a micro-macro constitutive model proposed by Cezard et al. (2005) and Favier et al. (2009) was used. Some preliminary results have been reported in Neag et al. (2014) but this paper presents a much fuller analysis.

2. Finite element simulation procedure

2.1. Geometry of the filling device

Fig. 1 shows a 3D view of the filling system used in the Atkinson et al. (2002) experiments. The cylindrical billet is 40 mm diameter and 45 mm height. The billet is first pushed into a vertical die, compressed by the upper part of the die and then turns 90° to enter into a 60 mm square Plate 7.5 mm thick. In some experiments, an obstacle was placed symmetrically in the die. Different shapes of obstacles were used (Table 1).

2.2. Mesh

In this work, the finite element code FORGE© was used to perform the numerical simulations. Only a half of the geometrical model (along the symmetrical plane) was meshed and considered

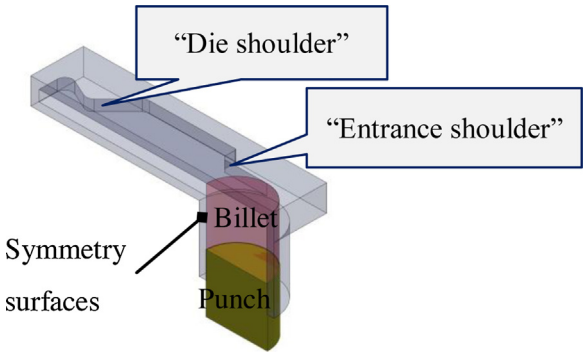

Fig. 1. Solid model of die filling system without an obstacle.

Table 1
Different shapes of obstacle used in this study (the terms 'standard spider' and 'experimental spider'originate from when obstacles with these geometries are used in polymer processing).

Circular		Standard spider	Experimental spider
Ø20 mm	Ø30 mm		

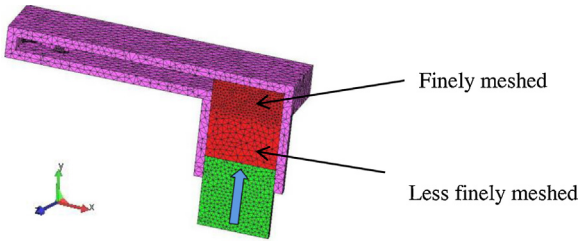

Fig. 2. The initial meshed view of the geometric model.

for calculations as the mechanical problem is symmetric in the flow direction. Using the multi-block technique, an adaptive volume meshing for the billet was applied on the region where the billet is severely deformed. These two mesh boxes were created in order to limit the element number and to ensure calculation accuracy for forming simulation. The billet is divided into 29497 tetrahedral elements and 6356 nodes, corresponding to a 0.7 surface shape factor (automatically checked by the GLPre Forge preprocessor). Up to 60% finer and coarser meshes were tested. The selected mesh provides similar strain rate and viscosity fields to those of the finer meshes while reducing the CPU time. The other parts of the geometrical model have coarser meshes. The die and the punch were assumed to be rigid bodies. The input parameters assigned to the deformed material are the initial temperature, the punch velocity (velocity at which the material enters in the mold), the friction coefficients and the parameters of the constitutive equations. The alloy was A357 aluminum alloy and the flow takes place under isothermal conditions. The initial temperature was chosen to be that associated with 0.5 solid fraction (from Liu et al. (2005)). The filling tests were carried out considering the mechanical parameters of a hydraulic press. Two ram velocities were used, 0.25 and 1 m s^{-1} (Fig. 2).

2.3. Modeling material behaviour and parameter identification

The constitutive equations adopted for this study are based on a micromechanical model proposed by Cezard et al. (2005) and Favier et al. (2009) which separates the role of four mechanical phases: the solid globules/agglomerates; the solid bonds between the solid globules; the free liquid; and liquid entrapped in the solid globules. The overall solid fraction is termed f^s. At rest, the solid globules tend to agglomerate leading to the formation of a 3D network. The

viscoplastic deformation is assumed to be accommodated by the solid bonds and the free liquid (Cezard et al., 2005; Favier et al., 2009; Favier and Atkinson, 2011). The solid agglomerates are presumed to deform very little though they contribute to an increase in the suspension viscosity. From a statistical point of view, the material is represented via a "coated inclusion". The "inclusion" is composed of both solid and liquid with volume fractions f_I^s and f_I^l, respectively ($f_I^s + f_I^l = 1$), with the latter representing entrapped liquid within the solid particles. The "coating" (the active zone that carries most of the deformation) consists of the solid bonds and the non-entrapped liquid with volume fractions f_A^s and f_A^l, respectively ($f_A^s + f_A^l = 1$).

f_I is the volume fraction of inclusion excluding the active zone and, in effect, gathers together all the phases that do not participate in the deformation. If f_A is the volume fraction of the active zone (the zone that mainly accommodates the deformation), then:

$$f_I + f_A = 1 \tag{1}$$

The evolution of the microstructure as a function of the strain rate, the overall solid fraction and time is captured through an internal variable. This internal variable is the solid fraction of the active zone f_A^s measuring the amount of bonds. The evolution law introduces agglomeration of solid particles (creation of solid bonds) and disagglomeration owing to shear inside the bonds (Eq. (2)).

$$\dot{f}_A^s = K_{ag} f^s \left(1 - f_A^s\right) - K_{dg} \left(1 - f^s\right) f_A^s \left(\sqrt{3}\dot{\epsilon}_{\mathrm{eq}}\right). \tag{2}$$

where K_{ag}, K_{dg} are the material parameters describing the agglomeration and disagglomeration mechanisms, respectively, and $\dot{\epsilon}_{\mathrm{eq}}$ is the macroscopic Von Mises equivalent strain rate ($\sqrt{3}\dot{\epsilon}_{\mathrm{eq}}$ is the corresponding equivalent shear rate). As a consequence, the steady-state solid fraction in the active zone is calculated by Eq. (3), as proposed by Favier et al. (2009):

$$f_{A\ \mathrm{steadystate}}^s = \frac{f^s}{f^s + K_{\mathrm{dg}}/K_{\mathrm{ag}}\left(1 - f^s\right)\left(\sqrt{3}\dot{\epsilon}_{\mathrm{eq}}\right)} \tag{3}$$

Solid fractions in the active zone higher than 0.4 represent semi-solids with a 3D continuous solid skeleton whereas solid fractions in the active zone lower than 0.4 represent liquid suspensions containing isolated agglomerates of solid (Favier et al. (2009) and Favier and Atkinson (2011)). The micro-macro modeling considers both liquid and solid phases as viscous, isotropic and incompressible and the following constitutive equations apply:

$$\underline{\underline{s}} = 2\eta\underline{\underline{\dot{\epsilon}}} \tag{4}$$

with

$$\eta = K_0\left(\epsilon_{\mathrm{eq}} + \epsilon_0\right)^n e^{-\beta T}\left(\sqrt{3}\dot{\epsilon}_{\mathrm{eq}}\right)^{m_s - 1} \quad \text{for the solid globules (in the "inclusion")} \tag{5}$$

$$\eta = K_p\left(\sqrt{3}\dot{\epsilon}_{\mathrm{eq}}\right)^{m_s - 1} \quad \text{for the solid bonds (in the "coating" also called active zone)} \tag{6}$$

$$\eta = K^l \quad \text{for the liquid phases} \tag{7}$$

$\underline{\underline{s}}$ and $\underline{\underline{\dot{\epsilon}}}$ are the deviatoric part of the stress and strain rate tensors and η is the viscosity, ϵ_{eq} is the von Mises equivalent strain, K_0, K_p and K^l are material constants, ϵ_0 is a constant used to manage the initial value of the solid consistency, T is the temperature, β is a material constant, m_s the strain rate sensitivity parameter of the solid phase and n is the strain hardening coefficient.

A self-consistent approximation is used at two scales to determine the semi-solid viscosity. First, the viscosities of the inclusion and of the active zone, associated with the respective volume fractions f_I and f_A, are calculated from the liquid and solid behaviour using a classical self-consistent scheme. Then the viscosity of the semi-solid is deduced from the inclusion and the active zone viscosities using the self-consistent estimation applied to the specific morphology of the coated inclusion. These homogenization steps do not require any additional parameters and were described in detail in Favier et al. (2009).

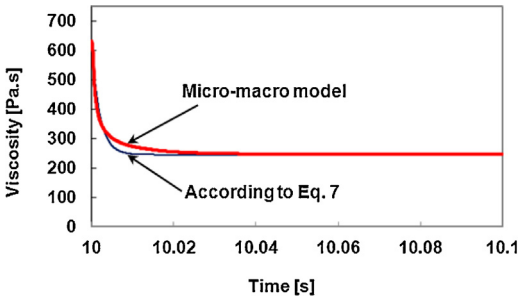

Fig. 3. Viscosity-time curve for 100 s^{-1} shear rate obtained from Eq. (8) and the micromechanical model. These curves were used for identifying the set of micromechanical model parameters (maximal error: 11.46%).

The set of material parameters were identified following the strategy used in Atkinson et al. (2002) who draw on experimental rapid compression tests carried out on A357 aluminium alloy slurry with 0.5 solid fraction (further described in Liu et al. (2003)). Atkinson et al. (2002) modelled those experiments using Flow-3D® CFD software. The ram speed range was 0.125 to 2 m s^{-1}. The instantaneous viscosity η over time t was represented via the exponential equation (Eq. (8)).

$$\frac{\eta - \eta_f}{\eta_i - \eta_f} = e^{-\left(a + b\left(\sqrt{3}\dot{\epsilon}_{\mathrm{eq}}\right)^q\right)t} \tag{8}$$

where η_i and η_f are the initial and the final (at steady state) viscosities, respectively, and a, b, q are material constants characterizing the deagglomeration process. The Cross equation was used with parameters adjusted from Yurko and Flemings (2002) and Loue et al., (1992). The other parameters were adjusted by fitting the load-displacement curve obtained for the rapid compression test carried out on A357 alloy at 0.5 m s^{-1} (Atkinson and Ward, 2002; Liu et al., 2003). A plot of viscosity *versus* time for 100 s^{-1} was derived from Eq. (8) (Fig. 3). For the Favier et al. (2009) micromechanical model parameters, a shear test at 100 s^{-1} was simulated. The set of model parameters was identified to obtain a good match between the predicted viscosity-time curve and the viscosity-time curve deduced from Eq. (8). The identification was realized considering that the initial solid fraction is homogeneous. Since the solid fraction is quite high and the material was at rest prior to the application of the load, it is assumed that there is a continuous solid skeleton initially within the material (by taking the initial solid fraction in the active zone $f_{A\mathrm{initial}}^s > f_c$=0.4 as in Favier et al. (2009) and Favier and Atkinson (2011); f_c is the percolation threshold for the solid phase). The values of the identified parameters are presented in Table 2.

As illustrated in Fig. 3, a good match between the two curves was obtained. The viscosity is found to decrease with time due to the deagglomeration process explicitly represented in the micro-

Table 2
Set of constitutive parameters used for simulations.

$f_{A\mathrm{initial}}^S$	$K_{ag}\,s^{-1}$	$K_{dg}\,s^{-1}$	f_A	f_c	K_0, K_p Pa.s	m_s	n	βK^{-1}	K^l Pa.s
0.7	0.2	10	0.03	0.4	6×10^4	0.22	0.01	0.4	1.81×10^{-2}

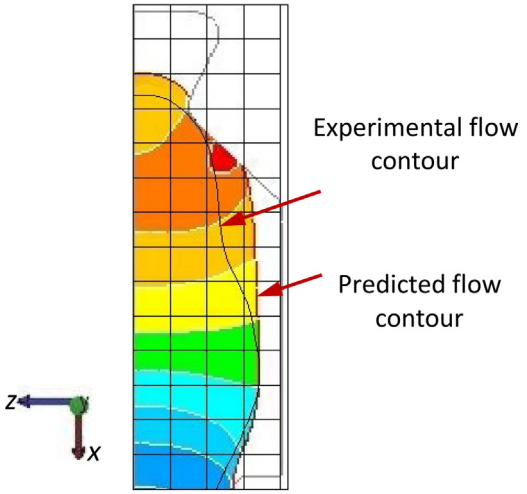

Fig. 4. Overlapping images to estimate the error between the predicted and experimental filling pattern.

macro model via Eq. (2). In the following, the set of parameters in Table 2 was used to simulate A357 semi-solid filling.

2.4. Modeling friction between the billet and the die

The contact between the billet and all the tools is modeled with a Coulomb law limited by Tresca which relates the shear stress τ and the normal stress σ_n. As the friction shear stress reaches a critical value related to the yield stress, it remains constant.

$$\tau = \mu\sigma_n \text{ if } \mu\sigma_n \leq m\frac{\sigma_0}{\sqrt{3}} \tag{9}$$

and

$$\tau = m\frac{\sigma_0}{\sqrt{3}} \quad \text{if } \mu\sigma_n > m\frac{\sigma_0}{\sqrt{3}} \tag{10}$$

where μ is the friction shear factor, m is the Tresca friction coefficient, and σ_0 the initial yield stress of the material.

The finite element code FORGE© allows different friction conditions to be entered in the calculation. An oil lubricant condition and a high friction condition corresponding to the friction parameters presented in Table 3 were analyzed.

2.5. Procedure to estimate the percentage of error between experimental and predicted flow front

To study the error between the predicted and experimental filling patterns, the images showing the material flow for a given punch displacement, coming from the experiment and the simulation, were superimposed and a statistical analysis was conducted. As an example, Fig. 4 shows a predicted filling pattern (presented in Fig. 6c) on which the experimental contour and a grid have been superimposed. Fifteen equally spaced grid points along the x axis of flow front and five equally spaced grid points along the z axis were considered. The lengths of grid lines on the x-axis and the z-axis for the experimental (l_{exp}) and the predicted (l_{pred}) flow front were measured to calculate the error. The local absolute relative error is $|\frac{l_{pred}-l_{exp}}{l_{pred}}|$. The overall error associated with a filling pattern was estimated by two mathematical representations: the average absolute relative error (AARE) and the root mean square percentage error (RMSPE) (Sabokpa et al., 2012; Srinivasulu and Jain, 2006). They were calculated using the following expressions:

$$\text{AARE}(\%) = \frac{1}{n}\sum_{i=1}^{n}\left|\frac{l_{ipred}-l_{iexp}}{l_{ipred}}\right| \times 100 \tag{11}$$

$$\text{RMSPE}(\%) = \sqrt{\frac{\Sigma_{i=1}^{n}\left(l_{iexp}-l_{ipred}\right)^2}{n}} \times \frac{100 \times n}{\Sigma l_{iexp}} \tag{12}$$

where n is the total number of employed data in the investigation.

Table 3
Friction parameters used for simulation.

Friction conditions	μ	m
Low friction (oil lubricant)	0.075	0.15
High friction	0.3	0.6

3. Results and discussion

3.1. Analyses of the die filling without and with obstacles

In this section, the effects of the elbow where the flow turns through a right angle to enter the die, and of the obstacle shape, on the semi-solid material flow behaviour are analysed. The punch velocity was 0.25 m s^{-1}. Both low and high friction coefficients were used.

3.1.1. Elbow effect on filling pattern

The predicted viscosity was found to strongly decrease when the flow turns through a right angle to enter the die (Fig. 5a). The blue and red colors are associated with the smallest and greatest values, respectively. Fig. 5b shows the distribution of the solid fraction in the active zone which is associated with the quantity of solid bonds in the micromechanical model. Fig. 5 exhibits results obtained for low friction coefficients. Similar results were observed with high friction coefficients.

Initially, the solid fraction in the active zone equals 0.7 indicating the presence of a continuous solid skeleton. It strongly decreases when the material is deformed and becomes lower than 0.4, suggesting that the solid skeleton was broken. The material is thus a liquid suspension containing isolated solid agglomerates. The viscosity decrease is clearly related to the breakdown of the solid agglomerates because of strong shear within solid bonds. The slurry behavior is controlled by the liquid and the semi-solid viscosity is high due to the presence of solid agglomerates.

3.1.2. Filling in the die without an obstacle

When the material is moving ahead in the horizontal plate and does not meet an obstacle, the experimental flow is coherent and can be divided into two stages. First the material flow is laminar and parallel with the die walls until reaching the "die shoulders" (the location of the "die shoulders" is defined in Fig. 1) (Fig. 6a). After the slurry meets the "die shoulders" (Fig. 6c and f), the end part of the die is filled. In the experiments the slurry 'swells' to fill the "entrance shoulders" (the location of the "entrance shoulders" is defined in Fig. 1). The experimental filling patterns, viewed from the top of the system, are compared with the predicted ones for both low and high frictions conditions (Fig. 6). The calculated results capture the experimentally observed filling quite well for both friction conditions during the first stage. More quantitatively, the average absolute relative error and mean square percentage error are about 8% during the first stage for both friction conditions (see Table 4). During this first stage, the material flows straight as demonstrated by the filling pattern and the velocity field. For the second stage (after the material meets the "die shoulder"), a better agreement between experiments and simulations was found with the high rather than the low friction coefficients. For low friction conditions, the AARE and the RMSPE increase with increasing displacement and reach 16% and 22%, respectively, for the 27 mm punch displacement

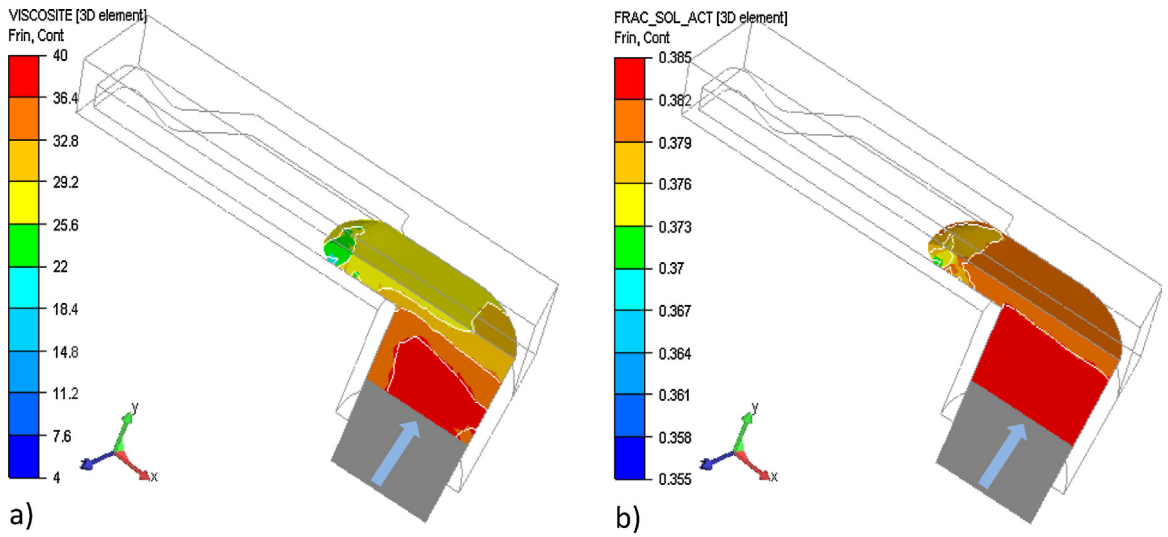

Fig. 5. Effect of elbow on filling pattern at 0.25 m s^{-1} and low friction coefficients: (a) viscosity (Pa.s); (b) solid fraction in the active zone, at 7 mm punch displacement.

(Table 4). For high friction conditions, the AARE and the RMSPE are lower and range from 6% to 10%.

The filling pattern and the velocity field reveal that as soon as the material meets the "die shoulder", the material flows to the sides of the die. High friction conditions between the material and the two top and bottom parts of the die emphasize this phenomenon. Consequently, the new material entering in the die is pushed to the die sides leading to the "swelling" phenomenon at the "die entrance", in

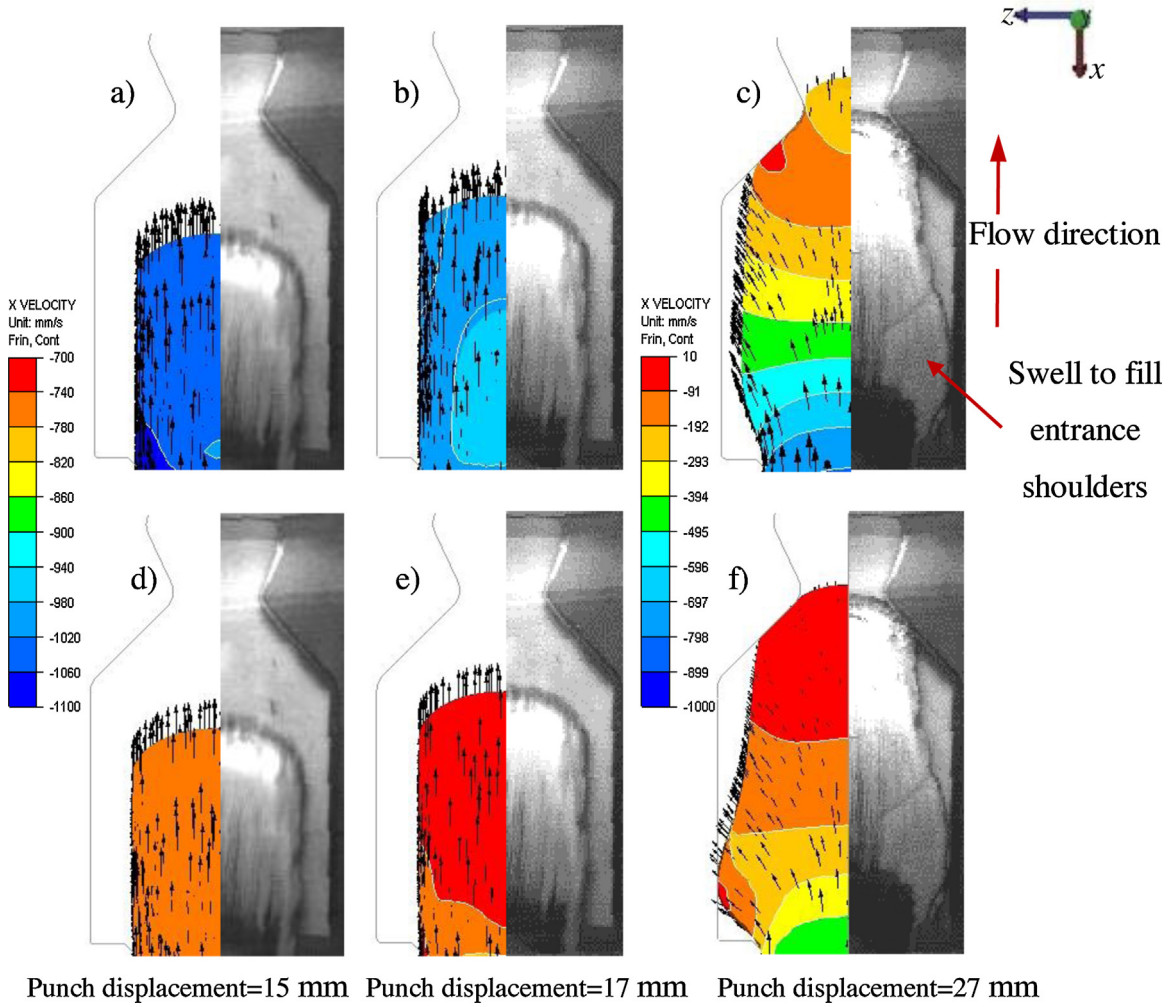

Fig. 6. Comparison of prediction and the experimental results for the filling of the die without an obstacle (top view): (a)–(c) before and after reaching the "die shoulders" for 0.25 m s^{-1} ram speed and low friction conditions; (d)–(f) before and after reaching the "die shoulders" for 0.25 m s^{-1} ram speed and high friction conditions.

Table 4
Values of AARE and RMSPE (errors between the predicted and experimental filling patterns) calculated for the cases "without an obstacle" presented in Figs. 6 and 11.

Punch displacement mm	Ram speed m s^{-1}	Friction conditions	AARE%	RMSPE%
17	0.25	Low friction	8	8
		High friction	8	8
	1	Low friction	15	17
		High friction	15	15
25	0.25	Low friction	13	14
		High friction	6	9
	1	Low friction	12	11
		High friction	15	16
27	0.25	Low friction	16	22
		High friction	9	10
31	1	Low friction	15	14

good agreement with experiments. Low friction conditions do not produce enough friction to get a "swelling" to a significant extent.

3.1.3. Filling in the die with circular obstacles

Fig. 7 presents the case of die filling with circular obstacles having two different sizes for 17 mm (Fig. 7a and b) and 21 mm punch displacement (Fig. 7c and d). Only the low friction condition is considered here. The larger diameter obstacle generated a thinner flow section beyond the obstacle (Fig. 7d). As a consequence, a larger zone, free from semi-solid, immediately beyond the obstacle, was created. Also, the "entrance shoulder" zone is more filled up by the material (Fig. 7b and d). As expected, as the size of the obstacle is increased, the material arrives sooner to the die end overflow (Fig. 7d). Finally, it is observed that after touching the "die shoulder" (Fig. 7d), filling of the die is almost immediate. No experiment with A357 semi-solid is available for circular obstacles. However, Atkinson et al. (2002) and Atkinson and Ward (2006) carried out experiments with both circular obstacles using semi-solid tin-lead alloy. The predicted filling patterns are consistent with their experimental observations.

3.1.4. Filling in the die with the experimental spider obstacle

Fig. 8 presents the case of die filling with an experimental spider obstacle. The results were obtained considering a ram speed of 0.25 m s^{-1} and low friction conditions (from a to c) and high friction conditions (from d to f). The AARE and the RMSPE are given in Table 5. In agreement with the experimental results, the slurry is deviated faster towards the walls of the die than without the obstacle (Fig. 8a). However, there are some discrepancies between the experimental and predicted filling patterns. The AARE and the RMSPE range between 18% and 21% for low friction coefficients and between 16% and 19% for high friction coefficients with increasing punch displacement. For low friction coefficients, the absolute relative error is the highest at the "entrance shoulders" where an insufficient "swell" of the slurry was also observed. Increasing the friction coefficients drastically reduces the errors: the AARE and the RMSPE both decrease to 2%. Consequently, as for the filling without an obstacle, much better qualitative and quantitative agreement was found when using the high friction conditions.

Table 5
Values of AARE and RMSPE calculated for the cases with "experimental spider obstacle" presented in Fig. 8.

Punch displacement	Friction conditions	AARE%	RMSPE%
15 mm	Low friction	18	21
	High friction	17	18
21 mm	Low friction	21	24
	High friction	16	17
23 mm	Low friction	21	21
	High friction	18	19

3.2. Punch velocity effect

Fig. 9 displays the filling patterns in the case of the experimental spider obstacle for two punch velocities, 0.25 m s^{-1} and 1 m s^{-1}. At low ram speed, the flow front is coherent and follows the obstacle shape. In Fig. 9a, the semi-solid slurry fronts rejoin after the experimental spider obstacle before reaching the "die shoulders". In contrast, at high ram speed, the semi-solid slurry reaches the "die shoulders" before the fronts rejoin (Fig. 9b).

Fig. 10 presents the predicted results obtained with the low friction conditions and the two punch velocities: 0.25 and 1 m s^{-1} in the case of the "experimental spider obstacle" (on the left in Fig. 10a and b) and the "standard spider obstacle" (on the right in Fig. 10c and d). At low ram speed, the flow follows very closely the edges of the experimental and standard spiders (Fig. 10a and c). This phenomenon is accentuated for the standard spider (Fig. 10c). At high ram speed, a different evolution of the flow was observed. The flow is relatively straight. All these results are in qualitative good agreement with experiments (compare Fig. 10b and d with Fig. 9b).

As expected for semi-solids, the viscosity of the material is on the whole lower as the ram speed is increased. Indeed, the solid phase viscosity decreases with increasing strain rate (Eq. (5)). Furthermore, suspended solid agglomerates disagglomerate faster (i.e. f_A^s decreases) with increasing strain rate (Eq. (2)), releasing some entrapped liquid. This phenomenon also contributes to a decreasing viscosity with increasing ram speed. The viscosity was found to be slightly affected by the friction coefficients at low ram speed but this effect vanishes at high ram speed.

Fig. 11 compares again experimental and predicted flow fronts obtained without an obstacle. Here, four cases were investigated: 0.25 m s^{-1} ram speed and low friction coefficients, 0.25 m s^{-1} ram speed and high friction coefficients, 1 m s^{-1} ram speed and low friction coefficients, 1 m s^{-1} ram speed and high friction coefficients. The AARE and the RMSPE values associated with these simulations are given in Table 4. The laminar flow observed during the first stage is not influenced by the ram speed. However some quantitative differences appear on the location of the flow front: the AARE and the RMSPE values are equal to 15% and 17% for 1 m s^{-1} and to 8% for 0.25 m s^{-1} for the 17 mm ram displacement. These values are very similar for both friction conditions. For the second stage, the AARE and the RMSPE values for low friction conditions are slightly lower for 1 m s^{-1} than for 0.25 m s^{-1} (12% and 11% compared to 13% and 14% for 25 mm ram displacement). However, the trend is opposite for high friction conditions: 15% and 16% for 1 m s^{-1} compared to 6% and 9% for 0.25 m s^{-1}. Therefore, comparisons of predicted and experimental flow patterns reveal that a better match is obtained for the high friction coefficients in the case of 0.25 m s^{-1} ram speed and for the low friction coefficients in the case of 1 m s^{-1} ram speed. The outlined box in Fig. 11 shows where there is closer agreement between experiments and modelling.

Fig. 12 compares experimental and predicted flow fronts in the case of the die containing the experimental spider obstacle. Similar observations as for the case of the die without an obstacle can be made: the best match between experiments and simulations are obtained for the couples "low ram speed - high friction coefficient" (Fig. 12a) and "high ram speed - low friction coefficient" (Fig. 12b).

3.3. Discussion of the ram speed and friction effects

Comparisons between the predicted and experimental filling patterns obtained for the 0.25 m s^{-1} punch velocity highlight the key role of friction in the fill in the "entrance shoulder" area, explaining the observed "swelling" (compare Fig. 11e and f).

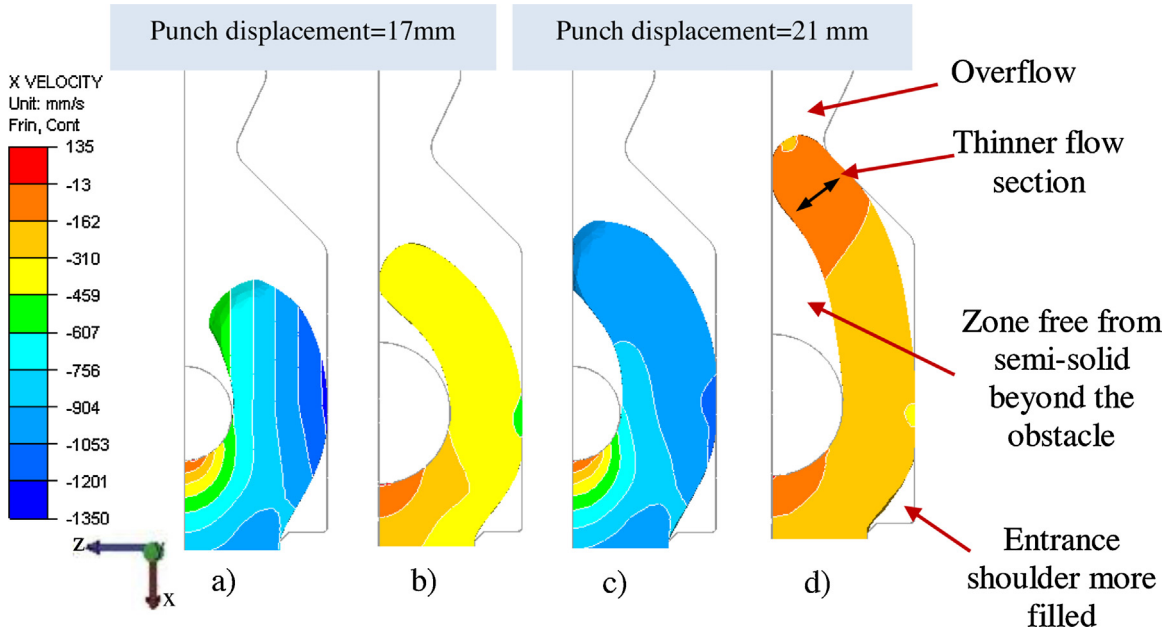

Fig. 7. Prediction for filling of the die with a circular central obstacle (top view): (a) Ø = 20 mm; (b) Ø = 30 mm at ram displacement of 17 mm; (c) Ø = 20 mm; (d) Ø = 30 mm at ram displacement of 21 mm.

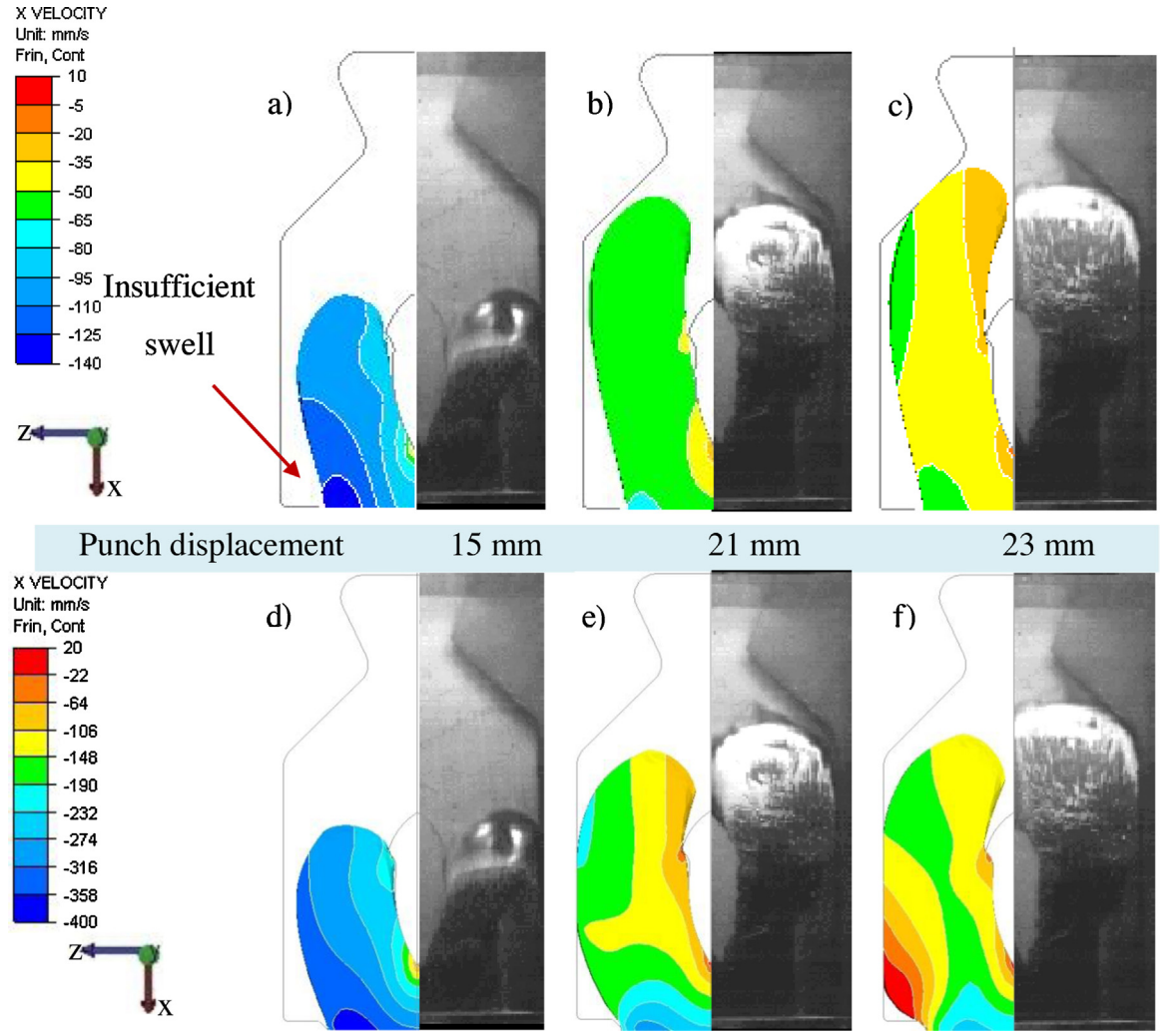

Fig. 8. Comparison of predicted and experimental filling of the die with an experimental spider obstacle (top view): (a)–(c) for 0.25 m s^{-1} punch speed and low friction conditions; and (d)–(f) for 0.25 m s^{-1} punch speed and high friction conditions.

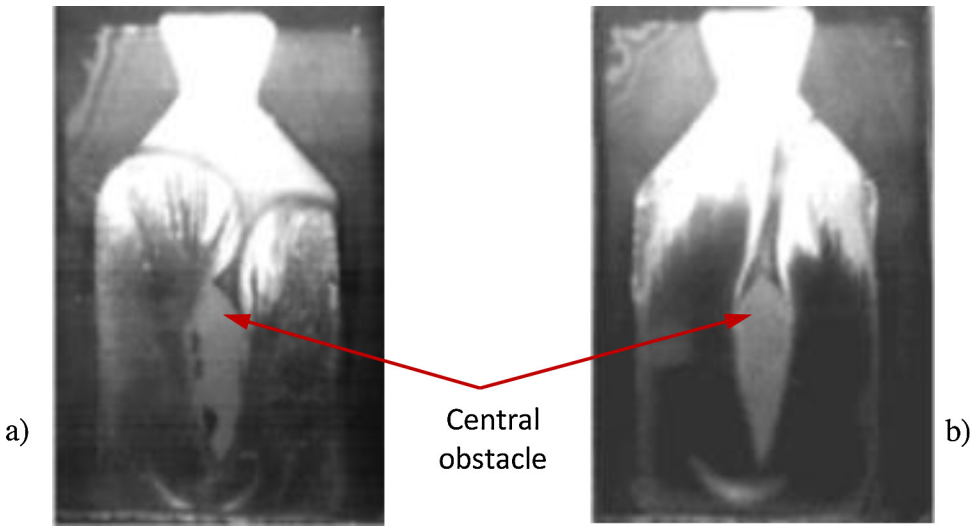

Fig. 9. Shots from filmed die filling with Al A357 in the case of the experimental spider obstacle: (a) 0.25 m s^{-1} ram speed; (b) the same at 1 m s^{-1}. These images are reported in Atkinson et al. (2002) and first published in Atkinson and Ward (2006).

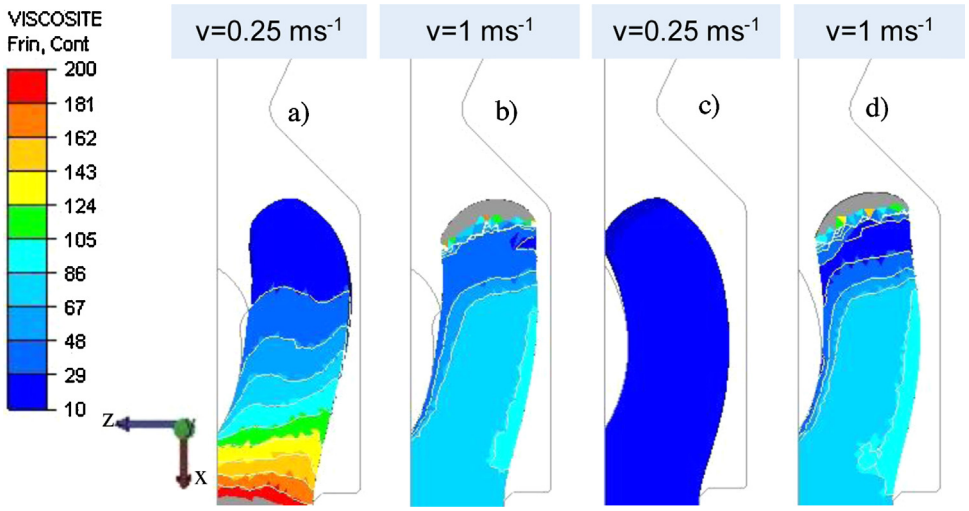

Fig. 10. Ram speed effect on die filling at 19 mm punch displacement—low friction coefficients (top view): (a) and (b) with experimental spider; (c) and (d) with standard spider. *Note*: the grey region at the top of the flow front corresponds to a region where the numerical equivalent strain rate falls down to zero leading to unrealistically high viscosities due to the shear thinning behavior of the material.

Stronger friction conditions result in better fill of the "entrance shoulders" From a process design point of view, this suggests that friction can be useful for filling of zones induced by strong change in section.

Fig. 13 presents the predicted von Mises equivalent strain rate fields obtained with the low and high friction coefficients and the two ram speeds: 0.25 and 1 m s^{-1} in the case of the die without an obstacle. As expected, increasing ram speed increases the strain rate of the semisolid slurry. As a consequence, the viscosity is lower for higher ram speed than for lower ram speed as illustrated in Fig. 11. However, the flow stress, which is the product of the viscosity, with the equivalent shear rate is higher. As the friction shear stress is proportional to the flow stress, it is higher for high than for low ram speeds for the same material and friction parameters.

In summary, friction modelling using the Coulomb law limited by Tresca (Eqs. (9) and (10)), classically used for hot forging, predicts a rise of friction magnitude with increasing ram speed. This rise leads to a strong effect of friction with regard to experiments for 1 m s^{-1} punch velocity: the friction coefficients have to be reduced to obtain a match with the experimental flow front for high ram speeds. As a result, it is concluded here that friction modelling using the Coulomb law limited by Tresca cannot represent the ram speed effect on experimental friction coefficients for the experiments developed in Atkinson et al. (2002).

The friction shear factor μ and the Tresca friction coefficient m are constant and, in particular, independent of the sliding velocity. This comes from the third rule of the sliding friction attributed to Coulomb (1785) but which is actually not valid (Bhushan (2013)). The coefficient of friction can increase with increasing relative sliding velocity (Gearing et al., 2001) or decrease with increasing sliding velocity for a certain velocity regime and/or the characteristics of the contact surface. The decrease of the friction with sliding velicity is called the Stribeck effect (Stribeck (1902) and Hersey (1914)). Several events can be responsible for the Stribeck effect. The Stribeck effect can be related to stick-slip motion due to the presence of asperity contacts (Rowson (1975) and Bhushan (2013)). A higher strenght of the sliding material could result in a lower real area of contact and so a lower friction coefficient (Bhushan (2013)). High sliding speeds and high shear rates can also result in increasing interface temperature leading to the melting of the

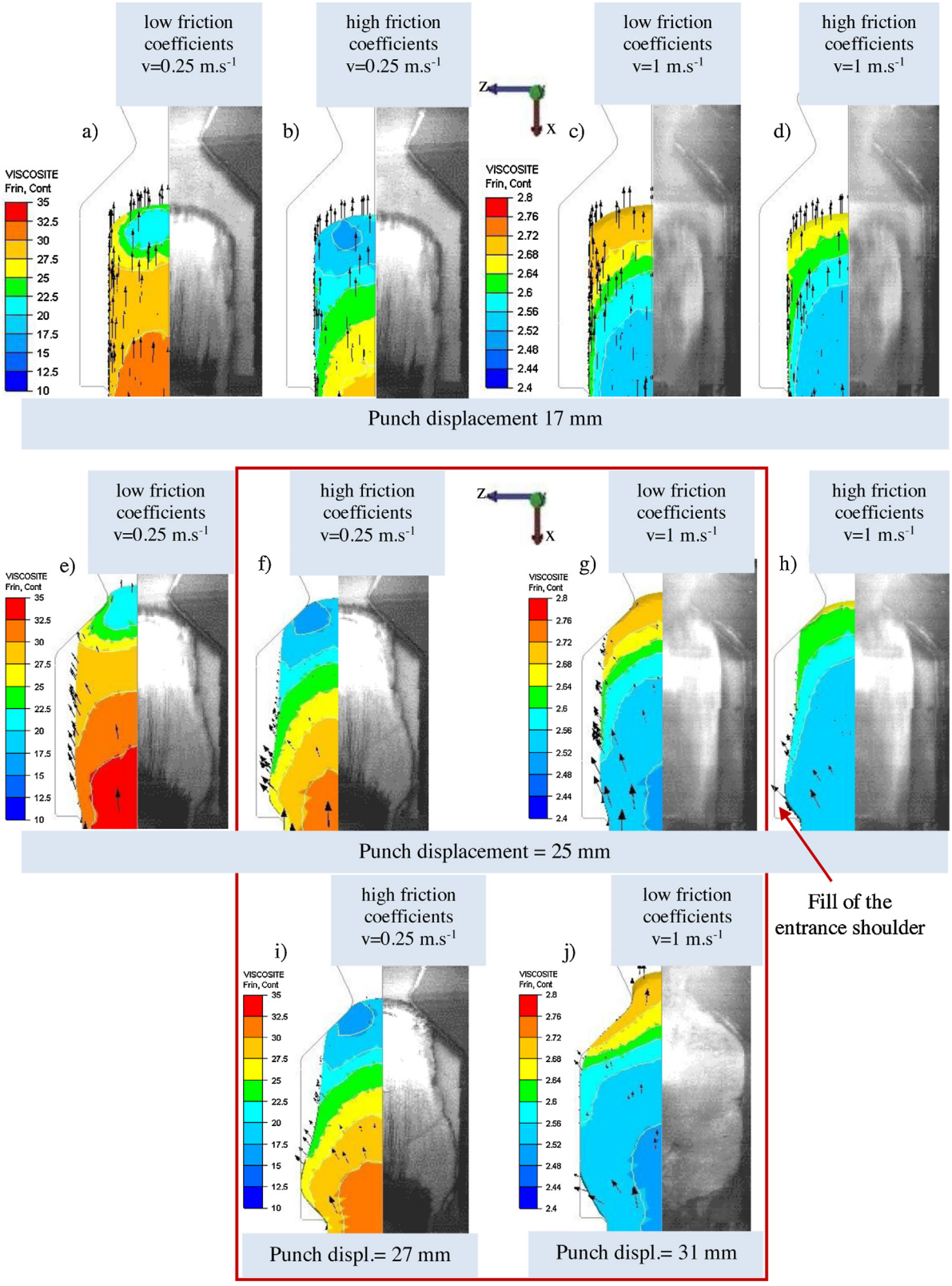

Fig. 11. Viscosity (Pa.s) evolution (top view): (a) low friction coefficients, ram speed 0.25 m s^{-1}; (b) high friction coefficients, ram speed 0.25 m s^{-1}; (c) low friction coefficients, ram speed 1 m s^{-1}; (d) high friction coefficients, ram speed 1 m s^{-1}; (e) low friction coefficients, ram speed 0.25 m s^{-1}, (f) high friction coefficients, ram speed 0.25 m s^{-1}, (g) low friction coefficients, ram speed 1 m s^{-1}, (h) high friction coefficients, ram speed 1 m s^{-1}, (i) high friction coefficients, ram speed 0.25 m s^{-1}, (j) low friction coefficients, ram speed 1 m s^{-1}.

material at the interface and the reduction in the friction coefficient (Bhushan (2013)), in a similar way to the aquaplaning phenomenon (Tuononen and Matilainen (2009)). The two last events mentioned above could explain why the friction conditions have to be reduced with an increase of the semi-solid velocity in the present study. The high velocity and the resulting higher shear rates can result in

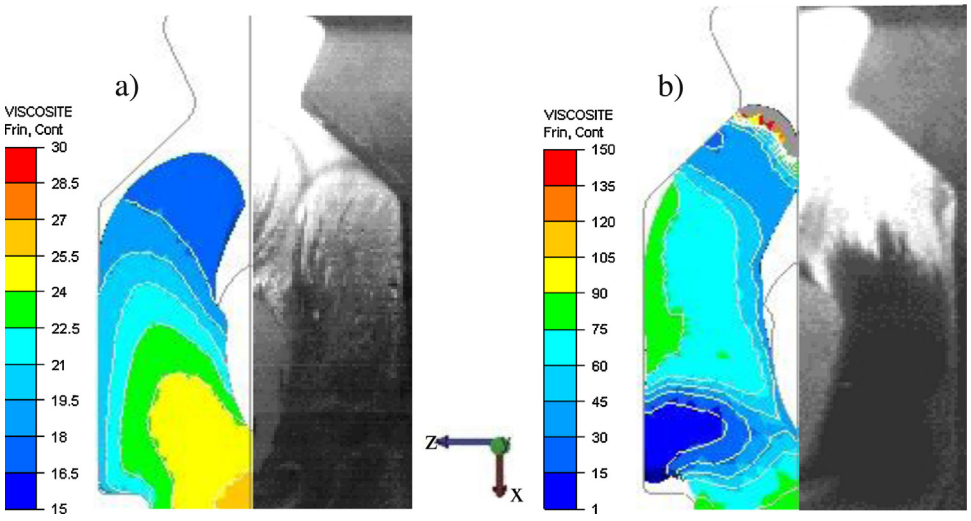

Fig. 12. Comparison of experimental and predicted filling of the die with the experimental spider obstacle (top view). Viscosity (Pa.s) map: (a) 0.25 m s^{-1}—high friction coefficients; (b) 1 m s^{-1}—low friction coefficients.

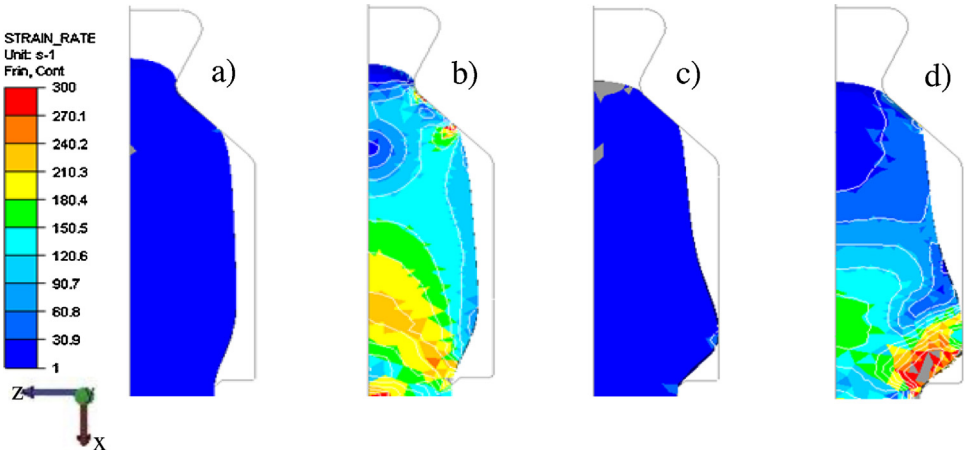

Fig. 13. Strain rate (s^{-1}) evolution: effect of the ram speed (top view): (a) 0.25 m s^{-1} and low friction coefficients; (b) 1 m s^{-1} and low friction coefficients; (c) 0.25 m s^{-1} and high friction coefficients; (d) 1 m s^{-1} and high friction coefficients.

a lower real area of contact and so a lower friction coefficient. A film with a higher volume fraction of liquid can be formed at the interface due to a temperature increase. Concerning the modelling of friction, on the contrary to the Coulomb model, the Norton-Hoff type laws, available in the FORGE© finite element code, relate the friction shear stress to the relative sliding velocity, in a similar way to the viscoplastic flow rule, but they are used to represent a positive rate sensitivity (Chenot et al., 2002). Several empirical models have been proposed to relate the friction coefficient to the relative sliding velocity, such as linear, exponential or polynomial in velocity to represent an negative rate sensitivity (Bhushan, 2013; Liu et al., 2013) and could be used to simulate the die filling with a 90° change of flow path as investigated in this paper. The temperature dependance of the friction coefficient could be also incorporated as proposed by Moufki et al. (1998) for cutting, or Assidi et al. (2010) for friction stir welding.

Summary

Die filling with a 90° change of flow path was simulated using the FORGE© finite element code and a constitutive equation based on micro-macro modelling. The predicted flow behaviour was compared to *in situ* flow visualization experimental data obtained with a transparent sided die in previously reported work (Atkinson et al., 2002; Atkinson and Ward, 2006). It was shown that:

- The initial solid skeleton is broken as soon as the material is deformed. The slurry in the horizontal plate of the die behaves as a suspension.
- The effect of an obstacle within the die on the material flow front is successfully predicted.
- The effect of ram speed on the material flow front is successfully represented by keeping the same parameters for the constitutive laws but requires a change in the friction coefficient.
- Friction modelling using the Coulomb law limited by Tresca cannot represent the ram speed effect on experimental friction conditions for the filling test developed in Atkinson et al. (2002).
- Stronger friction conditions result in better filling of the die 'entrance shoulders' *i.e.* those regions which tend to be voids because of a severe change in section.

Acknowledgements

Professor Atkinson would like to thank Arts et Métiers Paris Tech for their invitation to be a Visiting Professor to carry out this work in collaboration with Professor Favier, and the University of Leicester

for permission to visit. The *in situ* flow visualisation experiments considered here but previously reported in Atkinson et al. (2002) and Atkinson and Ward (2006) were carried out at the University of Sheffield funded by the Engineering and Physical Sciences Research Council of the UK.

References

Assidi, M., Fourment, L., Guerdoux, S., Nelson, T., 2010. Friction model for friction stir welding process simulation: calibrations from welding experiments. Int. J. Mach. Tools Manuf. 20, 143–155.

Atkinson, H.V., 2005. Modelling the semisolid processing of metalllic alloys. Prog. Mater. Sci. 50, 341–412.

Atkinson, H.V., Ward, P.J., Kapranos, P., Liu, T.Y., Chin, S.B., Kirkwood, D.H., 2002. Final Report for EPSRC Project: Modelling of Thixotropic Flow of Metal Alloys into a Die—GR/M17334/01, (http://www2.le.ac.uk/departments/engineering/people/academic-staff/helen-atkinson).

Atkinson, H.V., Ward, P.J., 2006. Flow visualization for semi-solid processing. JOM 58 (6), 21–23.

Bhushan, B., 2013. Introduction to Tribology. Wiley & Sons, New York.

Cezard, P., Favier, V., Bigot, R., Balan, T., Berveiller, M., 2005. Simulation of semi-solid thixoforging using a micro-macro constitutive equation. Comput. Mater. Sci. 32, 323–328.

Chenot, J.L., Fourment, L., Mocellin, K., 2002. Numerical treatment of contact and friction in FE simulation of forming processes. J. Mater. Process. Technol. 125-126, 45–52.

Coulomb, C.A., 1785. Théorie des machines simples. Mem. Math. Phys. Acd. Sci. 10, 161–331.

Favier, V., Cezard, P., Bigot, R., 2009. Transient and non-isothermal semi-solid behaviour: 3D micromechanical modeling. Mater. Sci. Eng. A 517, 8–16.

Favier, V., Atkinson, H.V., 2011. Micromechanical modelling of the elastic–viscoplastic response of metallic alloys under rapid compression in the semi-solid state. Acta Mater. 59, 1271–1280.

Flemings, M.C., 1991. Behavior of metal alloys in the semisolid state. Metall. Trans. A 22A, 957–981.

Gearing, B.P., Moon, H.S., Anand, L., 2001. A plasticity model for interface friction: application to sheet metal forming. Int. J. Plast. 17, 271–273.

Hersey, M.D., 1914. The laws of lubrication of horizontal journal bearings. J. Wash. Acad. Sci. 4, 542–552.

Hufschmidt, M., Modigell, M., Petera, J., 2006. Modelling and simulation of forming processes of metallic suspensions under non-isothermal conditions. J. Non-Newtonian Fluid Mech. 134, 16–26.

Liu, Y., Pavlovskaia, E., Hendry, D., 2013. Vibro-impact responses of capsule system with various friction models. Int. J. Mech. Sci. 72, 39–54.

Ito, Y., Flemings, M.C., Cornie, J.A., 1992. Nature and Properties of Semi-solid Materials. TMS, Warrendale, P.A, pp. 3–17.

Jorstad, J., Alexandrou, A.N., Mitsoulis, E., 2014. Semi-solid metal processing: unlimited flow velocity without turbulence in thin cast sections. Solid State Phenom. 217-218, 159–165.

Kang, C.G., Lee, S.M., Kim, B.M., 2008. A study of die design of semi-solid die casting according to gate shape and solid fraction. J. Mater. Process. Technol. 204, 8–21.

Koeune, R., Ponthot, J., 2014. A one phase thermomechanical model for the numerical simulation of semi-solid material behavior. Application to thixoforming. Int. J. Plast. 58, 120–153.

Liu, T.Y., Atkinson, H.V., Kapranos, P., Kirkwood, D.H., Hogg, S.C., 2003. Rapid compression of aluminium alloys and its relationship to thixoformability. Metall. and Mater. Trans. A 34A, 1545–1554.

Liu, D., Atkinson, H.V., Jones, H., 2005. Thermodynamic prediction of thixoformability in alloys based on the Al–Si–Cu and Al–Si–Cu–Mg systems. Acta Mater. 53, 3807–3819.

Loue, W.R., Suery, M., Querbes, J.L., 1992. Microstructure and rheology of partially remelted AlSi-alloys. In: Proc. 2nd Int. Conf. on the Semi-Solid Processing of Alloys and Composites, Cambridge, Massachussets, pp. 266–275.

Maciol, P., 2009. Application of internal variable convection for modelling of T-shape mould filling. Arch. Civil Mech. Eng. 9, 67–74.

Moufki, A., Molinari, A., Dudzinski, D., 1998. Modelling of orthogonal cutting with a temperature dependent friction law. J. Mech. Phys. Solids 46, 2103–2138.

Neag, A., Favier, V., Bigot, R., Atkinson, H.V., 2014. Analysis by micromechanical modeling on material flow under rapid compression in the semi-solid state. Solid State Phenom. 217-218, 182–187.

Sabokpa, O., Zarei-Hanzaki, A., Abedi, H.R., Haghdadi, N., 2012. Artificial neural network modeling to predict the high temperature flow behavior of an AZ81 magnesium alloy. Mater. Des. 39, 390–396.

Rowson, D.M., 1975. An analysis of stick-slip motion. Wear 31, 213–218.

Solek, K., Stuczyński, T.B., ialobrzeski, A., Kuziak, R., Mitura, Z., 2005. Modelling thixocasting with precise accounting of moving front of material. Mater. Sci. Technol. 215, 551–558.

Spencer, D.P., Mehrabian, R., Flemings, M.C., 1972. Rheological behaviour of Sn15%Pb in the crystallization range. Metall. Trans. A 3, 1925–1935.

Srinivasulu, S., Jain, A., 2006. A comparative analysis of training methods for artificial neural network rainfall–runoff models. Applied Soft Computing 6 (3), 295–306.

Stribeck, R., 1902. Die wesentlichen Eigenschaftender Gleitund Rollenlager—the key qualities of sliding and roller bearings. Zeitschrif tdes Vereines Deutscher Ingenieure 46, 1342-8–1432-7.

Tuononen, A.J., Matilainen, M.J., 2009. Real-time estimation of aquaplaning with an optical tyre sensor Institution of Mechanical Engineers, Part D. J. Automob. Eng. 223, 1263–1272.

Yurko, J.A., Flemings, M.C., 2002. Rheology and microstructure of semi-solid aluminum alloys compressed in the drop-forge viscometer. Metall. Mater. Trans. A 38, 2737–2746.